JACS
JOURNAL OF THE AMERICAN CHEMICAL SOCIETY

Article

pubs.acs.org/JACS

# Oxidative Nanopeeling Chemistry-Based Synthesis and Photodynamic and Photothermal Therapeutic Applications of Plasmonic Core-Petal Nanostructures

Amit Kumar,[†] Sumit Kumar,[†] Won-Kyu Rhim, Gyeong-Hwan Kim, and Jwa-Min Nam*

Department of Chemistry, Seoul National University, Seoul 151-747, South Korea

Supporting Information

**ABSTRACT:** The precise control of plasmonic nanostructures and their use for less invasive apoptotic pathway-based therapeutics are important but challenging. Here, we introduce a highly controlled synthetic strategy for plasmonic core-petal nanoparticles (CPNs) with massively branched and plasmonically coupled nanostructures. The formation of CPNs was facilitated by the gold chloride-induced oxidative disassembly and rupture of the polydopamine corona around Au nanoparticles and subsequent growth of Au nanopetals. We show that CPNs can act as multifunctional nanoprobes that induce dual photodynamic and photothermal therapeutic effects without a need for organic photosensitizers, coupled with the generation of reactive oxygen species (ROS), and allow for imaging and analyzing cells. Near-infrared laser-activated CPNs can optically monitor and efficiently kill cancer cells via apoptotic pathway by dual phototherapeutic effects and ROS-mediated oxidative intracellular damage with a relatively mild increase in temperature, low laser power, and short laser exposure time.

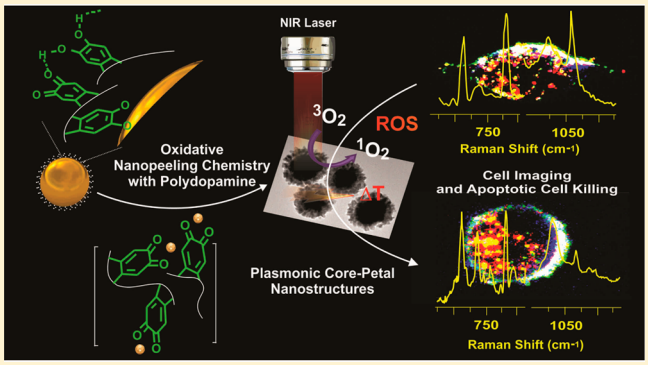


## INTRODUCTION

Plasmonic metal nanostructures have been drawing enormous attention for their strong and controllable optical properties and potential use in biosensing, bioimaging, and therapeutic applications.[1−10] Near-infrared (NIR) light-mediated phototherapeutic approaches with these plasmonic nanostructures, such as photodynamic therapy (PDT)[11,12] and photothermal therapy (PTT),[5−7] have shown several advantages including high spatial resolution, improved target selectivity, reduced side effects, noninvasiveness without a need for surgery, fast and effective treatment, and low cost over conventional cancer therapies. PDT involves the use of organic photosensitizer (PS) molecules which use the site-selective exposure of a specific light wavelength to convert normal tissue oxygen ($^3O_2$) to the very reactive and cytotoxic singlet oxygen ($^1O_2$).[11] For a highly efficient PDT, this light wavelength needs to match the maximum absorption wavelength of a PS within the NIR region (700−1100 nm; phototherapeutic NIR window to avoid interference with blood and tissue).[13] Unfortunately, most of the therapeutic PS molecules absorb light in the visible region and are prone to photodecomposition under long-term light exposure,[14,15] and prolonged PDT treatment creates severe local hypoxia by depletion of tissue oxygen, hampering further PDT operation.[16,17] On the other hand, the PTT methods use plasmonic nanoparticles, such as gold nanoparticles (AuNPs), that induce hyperthermia and/or subsequent small shock waves by exposure to a continuous wave or pulsed laser, resulting in apoptotic or necrotic cancer cell death depending on the increase in the local temperature.[5−7] The efficient hyperthermal necrotic destruction of cancer cells involves very high temperature (>70 °C),[18] causing collateral damage to healthy cells and also undesirably reshaping nanostructures.[19,20] For less invasive cancer cell death, it is advantageous to use a low-temperature-based (<45 °C) PTT strategy. Further, under a prolonged treatment condition, cancer cells can acquire resistance that hampers further treatment.[21]

For these reasons, recently, there have been the efforts toward the development of PDT−PTT integrated platforms that involve visible/NIR light-absorbing hybrid nanostructures from PTT-active structures such as Au nanoflowers, Au nanorods (AuNRs), Au nanocages, and graphene oxides, and PDT-active PS molecules.[22−30] These hybrid nanostructures allow the use of moderate hyperthermia along with reactive oxygen species (ROS)-mediated intracellular damage. There are still several challenges, including the possible mismatch between the absorption wavelengths of PS and plasmonic nanostructures, the energy transfer between PS and nanostructures, the requirement of lower operation temperature or nonthermal treatment, the toxicity of nanostructures, and the complex conjugation chemistry, which all need to be addressed for the full utilization of these hybrid nanostructure-based approaches for practical applications. In particular, an effective photothermal nanotransducer should have a high optical

**Received:** August 20, 2014
**Published:** November 11, 2014

   dx.doi.org/10.1021/ja5085699 | J. Am. Chem. Soc. 2014, 136, 16317−16325

absorption cross-section, biocompatibility, and easy synthesis and a high structural precision and synthetic yield and plasmonic tunability in the NIR region.[31−38] So far, there has been little effort toward the ROS generation capability of NIR-active plasmonic nanostructures in combination with their inherent hyperthermic effect for potential NIR laser-based cancer phototherapy without the need for additional organic PS molecules.[39,40]

Branched plasmonic nanostructures, such as nanostars, nanoflowers, and nanolaces, can form strong electromagnetic (EM) fields inside particles due to their closely positioned and coupled sharp nanofeatures. These strong plasmonic couplings and large surface areas are useful features for surface-enhanced Raman scattering (SERS), photothermal conversion, and catalysis.[41−46] These branched plasmonic nanostructures could be promising PDT and PTT substrates, but the solution-phase large-scale synthesis to grow such anisotropically branched Au nanostructures with high structural precision and controllability is challenging due to the high diffusion coefficient of Au atoms and their face-centered cubic faceting tendency.[47,48] The anisotropic growth of these nanobranches seldom occurs when the reaction is kinetically controlled, and the growth of high-energy facets is faster than low-energy facets. Further, it is difficult to optimize such reaction conditions with varying surfactants in order to produce structurally reproducible homogeneous nanostructures in a large number.[41,47−52]

Here, we introduce the oxidative nanopeeling chemistry of polydopamine (pdop) for the controlled growth and synthesis of plasmonic nanobranched structures with tunable structural features and density on the surface of pdop-coated spherical AuNPs (Figure 1a). The thermoplasmonic property-based multifunctionalities of these Au core-petal nanoparticles (CPNs) were explored for the PDT−PTT dual photothermal therapeutics along with their ROS-based therapeutic effects. Further, the plasmonic couplings between the nanobranches of CPNs were used for SERS-based monitoring of the changes in DNA of cells of interest. The pdop layer can be stably and uniformly assembled on the Au core surface,[53−56] and Au(III)-induced oxidation of the catechol moieties of pdop triggers the partial disassembly of the pdop layer on the AuNP core and facilitates the anisotropic growth of petal nanostructures with various protrusion lengths and densities. The CPNs with different branching morphologies are highly controllable and exhibit wide optical spectra from visible to NIR regions depending on petal protrusion length and density. The local photothermal heating of 0.5 nM CPNs with densely protruded petals in aqueous solution to 53.7 °C was achieved within 6 min using a 785 nm laser of 2 W/cm$^2$, and it was also observed that $^1O_2$ was generated in aqueous solution during this process. We further studied the CPNs for their phototherapeutic potential with human cervical cancer cells (HeLa cells). It was confirmed by dark-field microscopic imaging and TEM that CPNs were efficiently taken up by HeLa cells in a large number (up to 1260 particles per cell; $10^4$ cells were measured) within 2 h, and these CPNs displayed no cytotoxicity. Under 785 nm laser exposure for 6 min, as many as 95% HeLa cells were killed at a moderate temperature (~42 °C). Such an efficient killing of cancer cells at a relatively low temperature is due to the synergistic combination of the photothermal effect and the plasmonics-assisted intracellular ROS generation. We also explored the intracellular structural and biochemical changes after phototherapeutic treatment of cancer cells in order to obtain a mechanistic insight in cell death. The TEM analysis of the fixed cells and nucleus-targeting dye-staining assay revealed severe damage to the cellular membrane and an apoptotic morphology of the cells. Further, a myriad of plasmonically coupled local hot spots inside the CPNs allowed for SERS-based analysis of ROS-mediated changes in DNA, and the results show that the oxidation and denaturation of DNA within CPN-containing cells were triggered by the exposure to 785 nm laser.

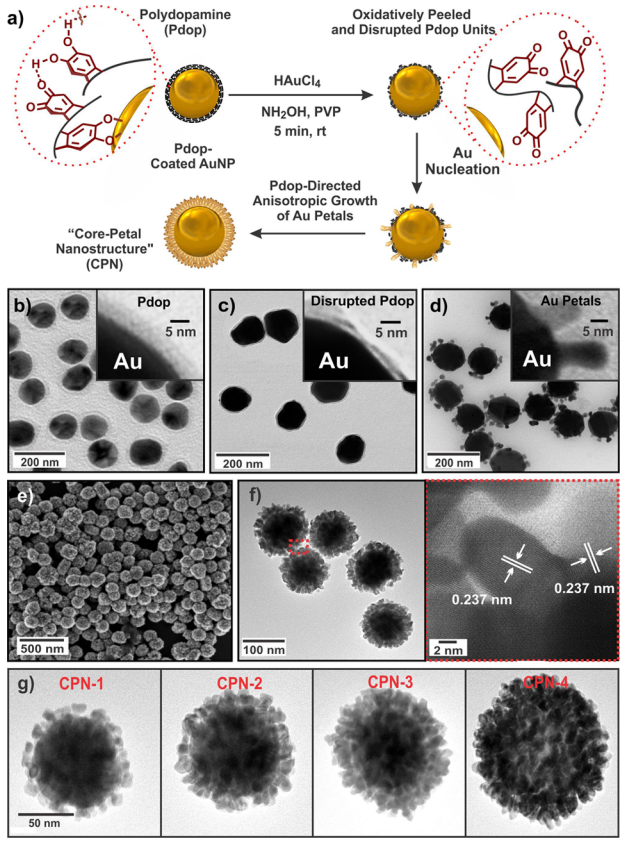


**Figure 1.** (a) Schematic representation for the oxidative nanopeeling chemistry of polydopamine (pdop) on AuNPs for the synthesis of plasmonic CPNs. (b) The TEM image of pdop-AuNPs with 80 nm Au core and ~5 nm pdop layer. (c) The TEM image of pdop-AuNPs immediately after adding $HAuCl_4$. (d) The TEM image after 1 min from adding $HAuCl_4$ to pdop-AuNPs. (e) The SEM image of CPNs. (f) The TEM image of CPNs (left) and the magnified petal image inside the red box (right). (g) The TEM images of CPN-1, CPN-2, CPN-3, and CPN-4, synthesized by increasing amounts of $HAuCl_4$ from left to right.

## RESULTS AND DISCUSSION

In a typical experiment, citrate-stabilized AuNPs (80 nm in diameter) were treated with dopamine·HCl in 10 mM Tris·HCl buffer at pH 8.5 for 4 h at room temperature to form 5 nm pdop-coated AuNPs (pdop-AuNPs) (Figure 1b; see the Experimental section for more details). The localized surface plasmon resonance (LSPR) band of pdop-AuNPs showed a small red-shift (~9 nm) (the LSPR bands for citrate-AuNPs and pdop-AuNPs are 522 and 531 nm, respectively), possibly due to the charge transfer between AuNP and pdop.[54] The pdop coating on AuNPs was also confirmed by X-ray photoelectron spectroscopy (XPS) (Figure S1). When the high-resolution Au 4f XPS spectra between pdop-AuNPs and


dx.doi.org/10.1021/ja5085699 | J. Am. Chem. Soc. 2014, 136, 16317−16325

citrate-AuNPs were compared, the 0.4 and 0.8 eV shifts of binding energies that correspond to Au $4f_{5/2}$ (83.6 eV) and Au $4f_{7/2}$ (87.1 eV), respectively, were observed (Figure S1). These data further support the binding of the catechol groups to AuNP surface.[57−59] In the presence of polymerization initiators (Tris) under alkaline conditions, dopamine was transformed to 5,6-dihydroxyindolines, their dione derivatives, and other related molecules, and these were closely packed due to strong supramolecular forces such as charge transfer, $\pi-\pi$ stacking, and hydrogen bonding to form a pdop layer on AuNPs.[60−63] For the synthesis of CPNs from pdop-AuNPs, 5 mL of 1 nM pdop-AuNP solution, 500 $\mu$L of $HAuCl_4$ (5 mM), 100 $\mu$L of PVP (5% w/v, 10,000 MW), and 500 $\mu$L of hydroxyl amine (50 mM) were added consecutively, and the reaction mixture was rigorously shaken for 5 min at 25 °C. The role of $HAuCl_4$ was studied with TEM, and the intermediate structures are shown in Figure 1c,d (the images show immediately after and 1 min after adding $HAuCl_4$). The oxidative disruption and peeling of the pdop layer on Au core and budding petal structures through the disrupted pdop layer were clearly observed (Figure 1c,d, respectively). The solution gradually changed color from red to blue, and the resulting blue-colored solution was stable for weeks, as confirmed by the UV−vis spectroscopy and TEM images, without showing any aggregation or subsequent change in color. The electron microscopic images of the sample revealed the formation of highly branched CPNs with closely positioned plasmonic petals on spherical Au cores (Figure 1e,f). The Raman spectra of pdop-AuNPs before and after $HAuCl_4$ treatment revealed the diminishing catechol peak at 1617 $cm^{-1}$ and the enhancement in quinone peak at 1651 $cm^{-1}$ (Figure S2). $HAuCl_4$-mediated oxidation of catechol to quinone was also confirmed by $^{13}C$ NMR where the signals at 142.9 and 143.7 ppm (catecholic carbon peaks) diminished, while the intensities of quinonic carbon signals at 182.0 and 183.7 ppm increased (Figure S3).[60] As shown in Figure 1a, the Au(III)-induced oxidations of catechols to quinones cause the disruption of the pdop assembly due to the absence of hydrogen bonds between the catechol and quinone groups, and the interaction between quinone and AuNP core is weaker than the binding between catechol and Au core (the TEM image of disrupted pdop is shown in Figure 1c). In this process, the budding Au nanopetal structures from Au core are grown on randomly oriented oxidized pdop-modified AuNP core, and subsequent reduction of remaining $HAuCl_4$ by hydroxyl amine fully triggers the anisotropic growth of Au petals (the budding Au petals are shown in Figure 1d). There are two major steps during the synthesis of CPNs: the oxidative disruption of pdop assembly on Au core and the reductive growth of Au petals through the disrupted pdop layer on Au core. Individual kinetics of these two steps is crucial for determining the final CPN structures. More disassembled pdop units result in high degree of petal protrusion. Higher amounts of hydroxyl amine linearly increased the reaction rate and produced smoother particle surfaces (Figure S4). Because Au(III) is needed to induce oxidation of the catechol moieties of pdop and disassemble the pdop layer, the faster reduction of Au(III) by larger amount of hydroxyl amine inhibits the oxidative nanopeeling of pdop, which in turn inhibits the formation of petals on Au core. On the other hand, when no hydroxyl amine was added, the complete oxidative peeling of pdop layer from Au core was observed (Figure S5). In a control experiment, we reacted citrate-stabilized 80 nm AuNPs with $HAuCl_4$ and $NH_2OH$ under the same conditions that were applied for the synthesis of CPNs from pdop-AuNPs. No protruding nanobranches were observed, but an increase in the diameter of spherical AuNPs from 80 to 83 nm was noticed. We then show that one can readily control the formation of the Au petals on Au cores and corresponding optical signals by simply varying the amount of $HAuCl_4$ (Figure 1g). It is clear that the number and length of the nanopetals increase as the amount of $HAuCl_4$ increases, and these changes also shift the LSPR peaks from the visible to the NIR region (Figure 2a; from CPN-1 to CPN-4).

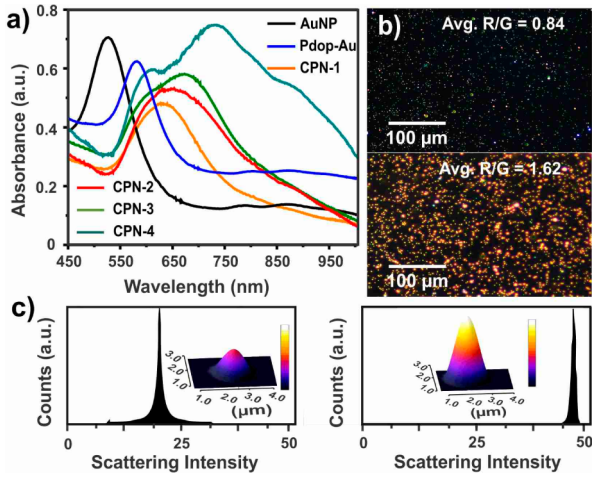


**Figure 2.** (a) UV−vis spectra of AuNPs, pdop-AuNPs, CPN-1, CPN-2, CPN-3, and CPN-4. (b) Dark-field microscopy image of pdop-AuNPs (upper) and CPN-4 (lower). (c) Comparison of scattering intensities and color spectrum obtained from pdop-AuNPs (left) and CPN-4 (right).

In particular, CPN-4 showed densely protruding nanopetals on the Au core, which can generate strong plasmonic coupling-based optical signals. It should be noted that a wide and strong spectrum from CPN-4 particles are desirable for biological applications due to the deep penetration depth of NIR light for biological samples. For the above reasons, we focused on CPN-4 particles for further studies. The UV−vis spectra of CPNs cover a broad range from the visible to the NIR region (530 to 975 nm) due to the multimodal couplings of the nanopetals of CPNs (Figure 2a).[51,52] Figure 2b represents the dark-field images of pdop-AuNPs and CPN-4 particles, respectively. A strong color change and scattering signal enhancement were observed when the CPNs with plasmonically coupled nanopetals were formed from pdop-AuNPs. The red-to-green color ratio (R/G) changed from 0.84 for pdop-AuNPs to 1.62 for CPN-4 particles. As shown in Figure 2c, the change in Rayleigh scattering can be attributed to the extensive plasmonic couplings between closely positioned metal nanobranches of CPN particles.[43] Our synthetic strategy gives a powerful and versatile pathway to a variety of branching nanostructures with different core sizes and branching morphologies. We synthesized CPNs with the core sizes of 10, 20, 30 and 50 nm, respectively, and all of these structures are near-infrared active, which is important for *in vivo* applications (Figure S6).

Next, we tested the potential use of CPNs as photothermal transducers for therapeutic applications (Figure 3a). Four different CPNs (CPN-1, CPN-2, CPN-3, and CPN-4) with increasing density of nanopetals were used for the experiments. First, a quartz cuvette, filled with CPN solution (12 $\mu$g/mL Au content from ICP-MS), was irradiated with a 785 nm laser


dx.doi.org/10.1021/ja5085699 | J. Am. Chem. Soc. 2014, 136, 16317−16325

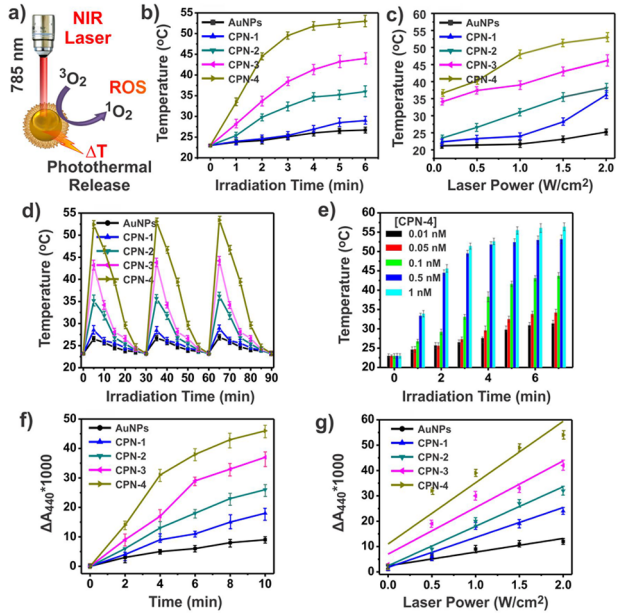


**Figure 3.** (a) Schematic representation of laser-induced photothermal effect and ROS production in a CPN. (b) Rise in temperature as a function of laser irradiation time for different gold nanoprobes. (c) Rise in temperature as a function of laser power for different gold nanoprobes. (d) Reproducibility test on the photothermal results with different gold nanoprobes in three successive cycles. (e) Increase in temperature as a function of time for different concentrations of CPN-4. (f) The RNO-histidine colorimetric assay-based results with different nanostructures for the quantification of laser-induced $^1O_2$ production while increasing laser irradiation time. (g) The RNO-histidine colorimetric assay-based results with different nanostructures for the quantification of laser-induced $^1O_2$ production while increasing laser power. All the error bars have been obtained from three repetitive experiments.

(2W/cm$^2$) from 0 to 10 min, and the temperature was measured by a thermocouple in the cuvette. As shown in Figure 3b, the temperature increased up to 53.7 °C from 23 °C when radiating the CPN-4 solution for 6 min (no temperature increase was observed afterward). From the results, we can conclude that the photothermal conversion was dependent on the density of the nanopetals of CPNs. It was also shown that with 6 min irradiation times, the solution temperature was linearly dependent on laser power (Figure 3c). In a control experiment with spherical AuNPs, poor photothermal response was observed under the identical irradiation conditions (785 nm, 2W/cm$^2$). To validate the stability of CPNs for photothermal heating, the photothermal heating−cooling process was repeated several times. In a typical experiment, the nanoparticle solution was exposed to a 785 nm laser for 5 min and allowed to cool down to room temperature for 30 min. This process was repeated three times. The results suggest that the photothermal heating process is completely repeatable with the identical heating−cooling profiles for all of the four different CPNs (Figure 3d). We confirmed that there was no noticeable structural change from CPN structures after three cycles of 5 min laser irradiations (Figure S7). In the case of CPN-4, we tested how particle concentration affects the photothermal heating. It was found that 0.5 nM CPN-4 solution with >4 min irradiation is needed to heat the solution to >50 °C, and, for heating the solution to >55 °C, 5 min heating of 1 nM CPN-4 solution is required (Figure 3e; 785 nm laser, 2 W/cm$^2$). We then checked the ability of CPNs for organic PS-free generation of ROS and subsequent PDT applications. It is known that gold nanostructures are involved with a plasmonic electron transfer to $^3O_2$ and can photosensitize the activation of $^3O_2$, for eventual conversion to $^1O_2$.[36,64−67] As proof-of-concept experiments, CPNs or AuNPs (1 nM concentration) were exposed to a 785 nm laser (2 W/cm$^2$) for 5 min, and the presence of $^1O_2$ was monitored by an *N*,*N*-dimethyl-4-nitrosoaniline (RNO)-histidine colorimetric assay (Figure 3f,g).[68] In this assay, the imidazole moiety of histidine reacts with $^1O_2$, and the resulting transient complex bleaches RNO molecules; the amount of $^1O_2$ can be directly correlated with a decrease in the RNO band intensity in the UV−vis spectrum. The generation of $^1O_2$ was characterized by analyzing the characteristic phosphorescence emission at ∼1268 nm upon exciting the CPN-4 nanoparticles in $D_2O$ with the light wavelength that matches with the LSPR of a nanostructure (Figure S8).[36,64,65] By purging the solution with nitrogen exhaustively, the phosphorescence emission at 1268 nm diminished, further supporting the presence of $^1O_2$ (Figure S8). As shown in Figure 3f,g, the amount of produced $^1O_2$ increases with longer laser exposure time or higher laser power. The maximum amount of $^1O_2$ was produced with CPN-4, while AuNPs generated the least amount of $^1O_2$ (785 nm laser, 2 W/cm$^2$), and this shows that $^1O_2$ production is highly dependent on the nanopetal structure and density. This laser irradiation-based $^1O_2$ production response pattern is very similar to the pattern of the CPN-based photothermal results. We also compared the performance of CPNs to AuNRs, widely used in photothermal and photodynamic therapeutics and plasmonics.[13] The AuNRs with the absorption maximum that matches with CPN-4 were synthesized using a literature method.[69] As shown in Figure S9, CPN-4 probes ($\Delta T$ = 23.7 °C) showed a much better photothermal effect than AuNRs ($\Delta T$ = 9 °C) under the same laser irradiation condition (785 nm source and 2 W/cm$^2$). It was also shown that CPN-4 produced approximately twice the amount of $^1O_2$ than AuNRs (Figure S9). It should be noted that Au content in AuNR or CPN-4 was kept same in these experiments. The sizes and lengths of the petals of different CPNs have been provided in Figure S10. It is well-known that more and stronger plasmonic coupling between metallic nanostructures can generate stronger EM field, and the size and shape of metallic nanostructure also affect the EM field of plasmonic nanostructures. We also performed the three-dimensional finite-element method (3D FEM) simulation (COMSOL, Stockholm, Sweden) to analyze the EM field distributions and enhancements of CPN and AuNR. As shown in the Figure S11, the EM field on a CPN is much stronger than that on an AuNR, mainly due to the petal structures and their massive plasmonic couplings on a CPN. Finally, the photothermal conversion efficiency ($\eta$) of CPN-4 was calculated to be 32%, which is clearly higher than AuNR (21%).[70]

We next tested CPNs for the potential use of cancer therapeutics applications with living cervical cancer cells (HeLa cells). First, we investigated the cells' internalization of nanoparticles. Typically, 1 nM nanoparticle solution was incubated with HeLa cells at 37 °C for 2 h, and excess CPNs were removed by washing the cells with PBS. The dark-field light-scattering images of the treated cells can directly visualize internalized CPNs. As shown in Figure 4b, the internalization of CPN-4 particles can be confirmed by the bright red-orange color inside the cells, while the dark-field images of the


dx.doi.org/10.1021/ja5085699 | J. Am. Chem. Soc. 2014, 136, 16317−16325

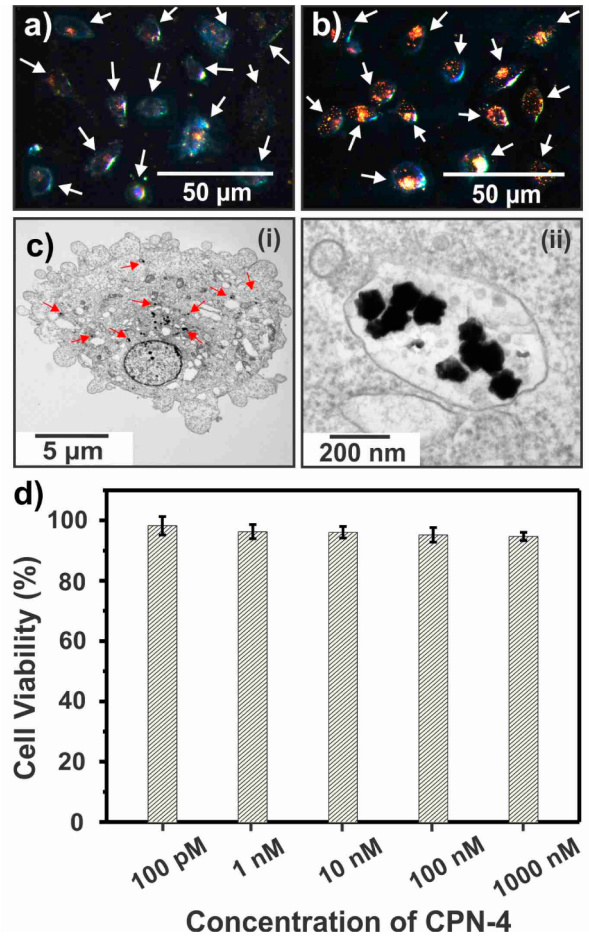


**Figure 4.** (a) The dark-field microscopy image of untreated HeLa cells. (b) The dark-field microscopy image of CPN-4-treated HeLa cells. (c) The low (i) and high (ii) magnification sectioned TEM images of a fixed HeLa cell, treated with CPN-4 probes. CPN-4 particles are encapsulated in endosomes. (d) HeLa cell viability assay results with different amounts of CPN-4 particles.

untreated cells show much weaker nanoparticle-scattering signals (Figure 4a). In order to reveal the exact location of CPNs inside the cells, CPN-4-treated cells were fixed, sectioned, and subjected to TEM. The TEM images show that CPN-4 particles were internalized by the cells and distributed in the cytosol (Figure 4c-i). A high-magnification TEM image revealed that CPN-4 particles were mainly located in endosomes, indicative of endocytosis (Figure 4c-ii). The average content of CPN-4 particles, present on the surface and inside the HeLa cells, was found to be ~1260 particles/cell by ICP-MS analysis, which is very high despite the fact that the size of CPN-4 particles is relatively large (~100 nm in diameter). This could be due to the branching shape effect that facilitates penetration of the cell membrane and the ionic screening effect by serum proteins in the cell growth medium and other cell membrane components.[51,71−73] Next, we performed the cytotoxicity test with HeLa cells using the Cell Counting Kit (CCK-8, Dojindo Lab, Japan). After incubation of the HeLa cells with different amounts of CPN-4 particles (100 pM to 1 $\mu$M) for 24 h, the cell viability results were obtained (Figure 4d). The results show that CPN-4 particles have negligible cytotoxic effects on HeLa cells, even at high probe concentrations (>100 nM). We then investigated the use of CPNs for dual PTT−PDT applications with NIR light. We first measured the photothermal response of CPN-4 as a function of laser irradiation time (785 nm, 2 W/cm$^2$) in cell growth medium (DMEM, 10% FBS, 1% antibiotic) up to 15 min, and it took nearly 10 min to increase the solution temperature to 54 °C (Figure S12). We confirmed via the UV−vis spectrometer that only negligible amount of CPN-4 particles aggregate in cell medium (Figure S13). Proteins, abundantly present in cell medium, can interact with nanoparticles,[74] and with laser-assisted photothermal heating, they can undergo conformational changes.[75] During this process, the heat from CPN probes can partially dissipate. This protein-based heat dissipation and a few nanoparticle aggregates can slow down the heating process. An increase in temperature to <45 °C with mild NIR laser power (~2 W/cm$^2$) is critical for clinical applications of PDT−PTT treatment to minimize the unnecessary heating of normal tissues.[76,77] The experiments were carried out with CPNs and spherical AuNPs. In a typical experiment, HeLa cells were incubated with 0.5 nM nanoparticle solution for 2 h, followed by irradiation with 785 nm laser (2W/cm$^2$) for 6 min, which results in temperatures increasing to 42 ± 1 °C. A colorimetric live/dead cell vitality assay kit (Invitrogen) was used to determine cell viability after irradiation. In Figures 5a and S14, the green and red-colored cells represent live and dead cells, respectively. The cell viability without nanoparticles was nearly 100% after 6 min laser irradiation, demonstrating that 6 min laser irradiation (785 nm laser; 2 W/cm$^2$) does not damage the cells when there are no plasmonic nanoparticles. The nanostructures with more

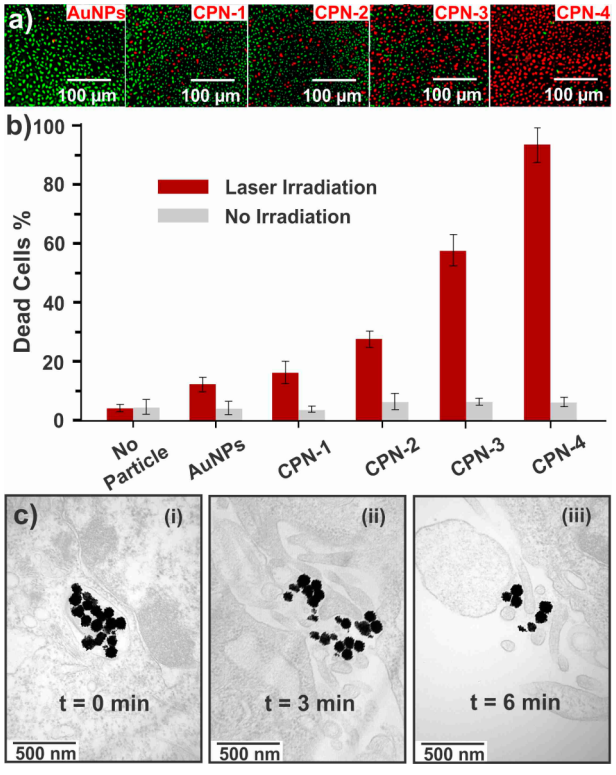


**Figure 5.** (a) The overlapped fluorescence images from the live/dead cell assays with HeLa cells. The green and red dots indicate live and dead cells, respectively. (b) HeLa cell death results from nanoparticle-based treatments with AuNPs, CPN-1, CPN-2, CPN-3, and CPN-4 in the presence or absence of laser irradiation. (c) High-magnification sectioned TEM images of a fixed HeLa cell, treated with CPN-4 particles and laser irradiation.


dx.doi.org/10.1021/ja5085699 | J. Am. Chem. Soc. 2014, 136, 16317−16325

protruding nanobranches induced cell death more efficiently when the cells were exposed to a 785 nm laser (Figure 5b). In particular, CPN-4 particles killed nearly all of the cancer cells after 6 min laser irradiation with an increase in temperature to ~42 °C. The sectioned TEM images of the fixed cells after exposing them to 785 nm laser with varying different irradiation times are shown in Figure 5c. It can be clearly seen that, in the absence of laser irradiation ($t$ = 0 min), CPN-4 particles are enclosed in the endosome. However, after irradiating cells with 785 nm laser for 3 and 6 min, the endosomes started to collapse, and the endosomal escape of CPN-4 particles was clearly observed (Figure 5c).

In the next set of experiments, we quantified the amount of ROS from nanoparticle-treated HeLa cells after laser irradiation using the OxiSelect assay (fluorescent signal-based method for measuring total ROS activity in cell lysates). The results show that the amount of ROS is correlated with differences in CPN structures (Figure 6c). This further suggests that CPN-4

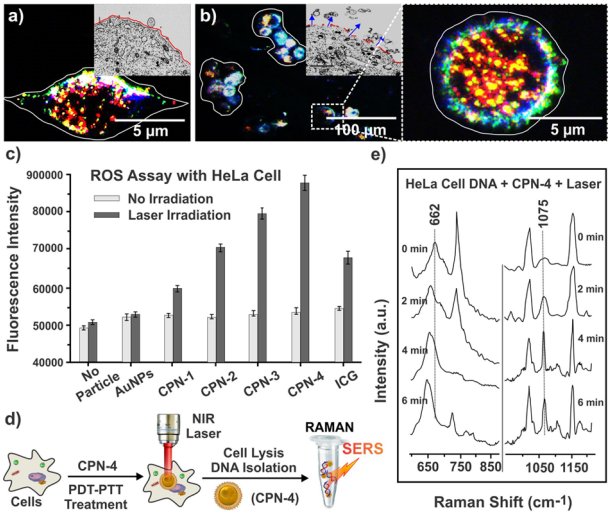


**Figure 6.** (a) The dark-field microscopic images of a live CPN4-treated HeLa cell without laser exposure (the inset TEM image shows an intact cellular membrane structure). (b) The dark-field microscopic image of dead HeLa cells, treated with CPN-4 particles, followed by laser exposure for the PDT–PTT treatment (the inset TEM image shows damaged cellular membrane). (c) ROS assay results from HeLa cell lysates after the PDT–PTT treatment using AuNPs, CPN-1, CPN-2, CPN-3, CPN-4, no particles (negative control) and ICG (positive control). (d) Schematic of genomic DNA isolation and SERS-based DNA characterization after the PDT–PTT-ROS treatment. (e) The Raman spectra of the isolated DNA from the PDT–PTT ROS-treated HeLa cells with CPN-4 particles (0, 2, 4, or 6 min laser exposure time).

particles can efficiently kill cancer cells with relatively mild increase in temperature (~42 °C) via PTT–PDT dual therapeutics. In order to quantify the photothermal and photodynamic contributions separately, we added different amounts of ascorbic acid (AA), a well-known antioxidant, during laser-induced cancer cell killing experiment.[37] After the addition of AA, cell viability kept increasing up to 82% (in the case of 500 $\mu$M AA) (Figure S15). It can be assumed that ROS production was ceased at >500 $\mu$M AA concentration, and the photothermal contribution is ~18% in this case. To further confirm, CPN-4 was coated with ~5 nm polydopamine layer to block $^1O_2$ production from Au surface (Figure S16). Indeed, polydopamine-coated CPN-4 could kill only ~17% cells (Figure S15). The ROS level, produced by CPN-4, has been compared to indocyanine green (ICG), a NIR absorbing PS.[39] As shown in Figure 6c, the ROS level in the presence of CPN-4 is 1.8-fold higher than the ICG case. We then probed the fate of cellular components that have been affected by light-induced PDT–PTT. Apoptotic cells can be directly monitored by fluorescence microscopy using ethidium bromide (EB), which stains the nuclei of dead cells because of the leaky nature of cell cytoskeleton and outwardly bulged cellular membrane.[67] In the presence of CPN-4 particles with laser irradiation, EB-treated HeLa cells exhibited intense red color, and the result indicates that the blebbing of the cell membrane was caused by the CPN-4-mediated PDT–PTT effect. After treatment with CPN-4 particles and laser irradiation, we observed changes in cell morphology from irregular ellipsoidal to circular shapes and aggregates from the dark-field microscope images (Figure 6b) due to the shrinkage of the cytoplasm and the contraction of the nucleus under high oxidative stress. The TEM image in Figure 6b reveals the formation of membrane bound vesicles in the cell membrane, and these vesicles are formed because of the translocation of phosphatidylserine from the cytoplasmic to the extracellular sides of the membrane.[78−80] Finally, we investigated the ROS-mediated change in nucleic acids using CPN-4 particles as SERS probes. The plasmonic CPN-4 structure with a highly branching morphology is an excellent SERS substrate. After treating HeLa cells with CPN-4 particles, the sample was exposed to a 785 nm laser for 2, 4, and 6 min, and genomic DNA was isolated with an extraction procedure as described in literature (Figure 6d).[81] The SERS signals were then used to study ROS-mediated primary and secondary structural changes in the isolated DNA (Figure 6e).[82] In a typical experiment, 10 $\mu$L of DNA solution (0.1 mg/mL) was mixed with 10 $\mu$L of 5 nM CPN-4 solution for the measurement of the SERS spectrum (it is known that DNA bases can interact with the Au surface).[51] $^1O_2$ and other intracellular secondary ROS are known to be mutagenic, genotoxic, and are involved in numerous biological processes. Hydroxyl radicals, excessively generated from lipid oxidation by singlet oxygen, may abstract the hydrogen atoms from the solvent-exposed regions of the sugar–phosphate DNA backbone, leading to $\beta$-cleavage of the strand and unstacking of DNA bases.[83] The phosphate-backbone-characteristic Raman peak ($PO^{2-}$ symmetric stretch) at 1082 $cm^{-1}$ was shifted to 1075 $cm^{-1}$, and its intensity was gradually increased in the CPN-4-treated sample as the exposure to the 785 nm laser increased. These changes occurred due to DNA phosphate-backbone damage and DNA aggregation. Another ROS-mediated chemical modification on DNA is the oxidation of DNA bases (i.e., the oxidation of guanine to result in 8-oxoguanosine lesion).[84,85] The Raman peak at 662 $cm^{-1}$ that corresponds to the radial-breathing vibration mode of guanine was shifted to ~649 $cm^{-1}$ after the PDT–PTT treatment. The shifted Raman band can be attributed to the preferred conformational change of *anti*-form in guanine to *syn*-form in 8-oxoguanine and also the change in the electronic environment due to the higher hydrogen bond occupancy of 8-oxoguanine as compared to guanine.[81] All these results suggest that there were chemical and structural changes in DNA inside the cells when the cells were treated with CPN-4 particles and 785 nm laser irradiation.

## ■ CONCLUSION

In summary, we reported the oxidative "nanopeeling" chemistry with a pdop organic corona to finely control plasmonic


dx.doi.org/10.1021/ja5085699 | J. Am. Chem. Soc. 2014, 136, 16317−16325

nanobranching on an Au core. We have shown that the plasmonic petals with highly controlled morphology, density, and plasmonic couplings between the protruding branches can be formed in a high yield by simply tuning the amount of gold-chloride and the reduction kinetics. Highly branched CPN structures exhibit an excellent NIR laser-based PDT−PTT theapeutic effect without a need for organic photosensitizers and can also be used as SERS probes for monitoring chemical and structural changes of the DNA in cells, mainly due to the CPN-4-induced generation of ROS. In particular, the efficient killing of cancer cells with CPN-4 particles and a 785 nm laser power density of 2 W/cm$^2$ within 6 min was possible with a mild increase in temperature to ∼42 °C. Our results suggest that the cause of CPN-4-based cell death is mainly due to cell membrane modification and the oxidative denaturation of nucleic acids, and the apoptotic killing of cancer cells is possible with CPN probes. We believe our strategy and results pave an avenue of highly controllable and reliable chemistry in forming plasmonically coupled nanobranch structures and offer insight and methods in PDT−PTT-based apoptotic therapeutics.

## EXPERIMENTAL SECTION

**Materials and Instruments.** All the chemicals were used as received without any further purification. Dopamine·HCl was purchased from Sigma-Aldrich (USA). Spherical AuNPs were purchased from BBInternational (USA). Hydrochloric acid and sodium hydroxide were purchased from Daejung Chemicals and Metals (Korea). Tris was purchased from USB Corporation (USA). The Formvar/carbon-coated copper grids were purchased from Ted Pella, Inc. (USA). Nanopure water (18.0 MΩ·cm) was used for all experiments. The UV−vis spectra were obtained from a UV−vis spectrophotometer (Agilent 8453 spectrophotometer, USA). Elemental analysis and binding energy measurements were performed using an X-ray photoelecton spectroscope (Axis HSi, KRATOS Analytical). The dynamic light scattering measurements were performed using a Malvern Zetasizer (Nano ZS). TEM images were obtained using an energy-filtering transmission electron microscope (LIBRA 120, Carl Zeiss) with an accelerating voltage of 120 kV. SEM images and EDS elemental mapping data were obtained using a field-emission scanning electron microscope (SUPRA 55VP, Carl Zeiss). The Raman spectra were acquired using a Renishaw inVia raman microscope equipped with 514, 633, and 785 nm laser sources.

**Polydopamine (pdop) Coating on 80 nm AuNPs.** One mL of commercially available colloidal solution of 80 nm citrate-stabilized AuNPs (11 pM) was centrifuged and redispersed in Tris·HCl buffer (pH 8.5, 10 mM). Five μL solution (5 mg/mL) of dopamine·HCl in Tris·HCl buffer (pH 8.5, 10 mM) was then added, and the reaction mixture was vortexed at 25 °C for 4 h. Finally, the reaction mixture was centrifuged at 8000 rpm for 5 min, and the supernatant was removed. The sediment containing pdop-AuNPs was then redispersed in DI water. The thickness of the pdop layer on an 80 nm Au core was estimated to be ∼5 nm from the TEM analysis.

**Synthesis of Gold CPNs.** For the synthesis of CPN-1, 5 mL of 1 nM pdop-AuNP solution, 50 μL of $HAuCl_4$ (5 mM), 100 μL of PVP (5% w/v, 10,000 MW), and 50 μL of hydroxyl amine (50 mM) were added consecutively, and the reaction mixture was rigorously shaken for 5 min at 25 °C. In order to synthesize CPN-2, CPN-3, and CPN-4, 100, 200, and 500 μL $HAuCl_4$ (5 mM), respectively, were used with hydroxyl amine (50 mM) solutions.

**Dark-Field Microscopy of pdop-AuNPs and CPN Probes.** Cleaned glass slides were treated with 2% (v/v) aqueous solution of 3-aminopropyl-trimethoxysilane (APTS) for 10 s, followed by washing with DI water and drying under nitrogen. Thereafter, 10 μL of a sample (pdop-AuNP or CPN, 0.1 nM) was loaded on the APTS-treated glass slide and sandwiched with a thinner glass slide. The dark-field images were obtained with a Carl Zeiss (DE/Axiovert 200) microscope.

**RNO-Histidine Assay.** Two mL CPN solution was added to a freshly prepared aqueous solution of RNO (50 μM) and 10 mM His (10 mL), and the mixed solution was transferred to a 1 mL quartz cuvette and irradiated with the laser (785 nm, 2 W/cm$^2$). The UV−vis absorbance at 440 nm was recorded at predetermined irradiation dosage.

**$^1O_2$ Luminescence Detection.** CPNs in $D_2O$ (1 mL) were subjected to laser irradiation, and the emitted luminescence was recorded. The measurements took place in the dark at a constant temperature of 15 °C by using a thermostat unit coupled to the detector.

**Cell Culture and Treatment with CPN Probes.** The HeLa cells were suspended in a 96-well plate at a concentration of $10^4$ cells/mL in Dulbecco's modified Eagle's medium (DMEM, 50 μL in each well) with 10% fetal bovine serum (FBS) and 1% antibiotic solution (GIBCO, Invitrogen, Karlsruhe, Germany) and cultured at 37 °C and 5% $CO_2$ overnight. The culture medium was then replaced with freshly prepared DMEM. Different concentrations of CPN solution in PBS were added, and the cells were left in a culture chamber for 2 h.

**Dark-Field Imaging of Live HeLa Cells.** HeLa cells were cultured on 35 mm polylysine-modified glass bottom culture dishes (MatTek Corp., USA) and allowed to grow in DMEM medium supplemented with 10% FBS and 1% antibiotics (37 °C, 5% $CO_2$) overnight. Next, the medium was replaced with fresh culture medium containing CPN nanoprobes (0.1 nM), and cells were further incubated for 2 h. Thereafter, the glass slide was washed with PBS to remove excess CPN nanoprobes, and the dark-field images were obtained with a Carl Zeiss (DE/Axiovert 200) microscope.

**Cell Cross-Section Imaging Using the Transmission Electron Microscopy.** For cell cross-section imaging, CPNs incubated cells were first detached from the well plate. After washing with PBS solution, >5 × $10^5$ cells were fixed for 2 h with modified Karnovsky's fixative (2% paraformaldehyde and 2% glutaraldehyde in 0.05 M sodium cacodylate buffer, pH 7.2). After repeated washing with 0.05 M sodium cacodylate buffer (pH 7.2) at 4 °C, cells were fixed with 1% osmium tetroxide in 0.05 M sodium cacodylate buffer (pH 7.2) for 2 h and then washed with distilled water two times. Fixed cells were En bloc stained at 4 °C overnight using 0.5% uranyl acetate and then dehydrated with a graded concentration series of ethanol (30%, 50%, 70%, 80%, 90%, 100%, 100%, and 100% ethanol; 10 min for each dehydration step). Infiltrated cells using propylene oxide and Spurr's resin were polymerized at 70 °C for 24 h. Various sections of the resin block were cut using an ultramicrotome (MT-X, RMC, Tucson, AZ, USA) and stained with 2% uranyl acetate and Reynolds' lead citrate for 7 min, followed by transferring the section of interest onto a 300 mesh copper TEM grid.

**Cytotoxicity Assay.** The cytotoxicity of various concentrations of CPNs was evaluated using the Cell Counting Kit (CCK-8, Dojindo lab., Japan). Cells were grown in a 96-well plate in 100 μL of DMEM supplemented with FBS. After 24 h seeding, cells were incubated with various concentrations (from 100 pM to 1 μM) of CPN-4 probes for 48 h, and the cell viability assay was carried out. The metabolic activity of the cells was measured using CCK-8 (a sensitive colorimetric assay for the determination of the number of viable cells after incubating with probes). Ten μL of the CCK-8 solution was directly added to the incubated cells in each well. After 2 h incubation at 37 °C, the amount of formazan dyes was measured by a microplate reader (Anthos 2010, Anthos Labtec, Eugendorf, Austria).

**Photothermal Therapy.** After incubation of the HeLa cells with CPNs, the cell monolayers were washed three times with PBS buffer and irradiated with a near-IR laser (785 nm, 2 W cm$^{-2}$, spot size of 5 mm). The cells were then incubated with 200 μL of fresh LIVE/DEAD reagent solution (LIVE/DEAD Viability/Cytotoxicity Kit, Molecular Probes) for 30 min in the dark. The green dots indicated healthy cells, while the red dots indicated dead cells.

**Genomic DNA Isolation.** After applying PTT using CPN-4 nanoprobes for 0, 2, 4, and 6 min, cells were lysed with 4 mL of lysis buffer containing 0.5 M Tris-HCl (pH 8.0), 20 mM EDTA, 10 mM NaCl, 1% SDS, and 0.5 mg/mL proteinase K. The mixture was incubated overnight at 55 °C. Two mL of saturated NaCl (6 M) was


dx.doi.org/10.1021/ja5085699 | J. Am. Chem. Soc. 2014, 136, 16317−16325

then added, and the samples were incubated at 55 °C for 10 min. After centrifugation at 5000 rpm for 30 min, the supernatant containing DNA was mixed with an excessive amount of chilled absolute ethanol, and the DNA was spooled by gently inverting the mix. The tubes were incubated at room temperature for 15 min, and the DNA was recovered by centrifuging at 10,000 rpm for 10 min at room temperature. The DNA was washed several times thoroughly with 70% ethanol and finally air-dried at room temperature.

**SERS Measurements of Isolated DNA using CPN-4 Probes.** The isolated DNA (10 μL, 0.1 mg/mL) from the HeLa cells after PDT−PTT treatment for different durations was mixed with CPN-4 nanoprobes (10 μL, 5 nM), and SERS spectra were recorded from the mixture on a glass slide using Reinshaw InVia Raman spectrometer with 785 nm laser and 50× objective lens.

## ■ ASSOCIATED CONTENT

### Ⓢ Supporting Information

XPS data, Raman spectroscopic data, TEM images, luminescence data. This material is available free of charge via the Internet at http://pubs.acs.org.

## ■ AUTHOR INFORMATION


### Corresponding Author

jmnam@snu.ac.kr

### Author Contributions

†These authors contributed equally.


### Notes

The authors declare no competing financial interest.

## ■ ACKNOWLEDGMENTS

This work was supported by the National Research Foundation (NRF) of Korea (2011-0018198) and the BioNano Health-Guard Research Center funded by the Ministry of Science, ICT & Future Planning (MSIP) of Korea as a Global Frontier Project (H-GUARD_2013M3A6B2078947). We acknowledge Dr. Kevin Hartman for his valuable suggestions during manuscript preparation.

## ■ REFERENCES


(1) Saha, K.; Agasti, S. S.; Kim, C.; Li, X.; Rotello, V. M. *Chem. Rev.* **2012**, *112*, 2739−2779.
(2) Wang, Y.; Bing-Yan, B.; Chen, L. *Chem. Rev.* **2013**, *113*, 1391−1428.
(3) Halas, N. J.; Lal, S.; Chang, W.-S.; Link, S.; Nordlander, P. *Chem. Rev.* **2011**, *111*, 3913−3961.
(4) Peer, D.; Karp, J. M.; Hong, S.; Farokhzad, O. C.; Margalit, R.; Langer, R. *Nat. Nanotechnol.* **2007**, *2*, 751−760.
(5) Qin, Z.; Bischof, J. C. *Chem. Soc. Rev.* **2012**, *41*, 1191−1217.
(6) Jain, P. K.; Huang, X.; El-Sayed, I. H.; El-Sayed, M. A. *Acc. Chem. Res.* **2008**, *41*, 1578−1586.
(7) Lal, S.; Clare, S. E.; Halas, N. J. *Acc. Chem. Res.* **2008**, *41*, 1842−1851.
(8) Wu, H.; Henzie, J.; Lin, W.; Rhodes, C.; Li, Z.; Sartorel, E.; Thorner, J.; Yang, P.; Groves, J. T. *Nat. Methods* **2012**, *9*, 1189−1191.
(9) Song, C.; Blaber, M. G.; Zhao, G.; Zhang, P.; Fry, H.; Christopher, S.; George, C.; Rosi, N. L. *Nano Lett.* **2013**, *13*, 3256−3261.
(10) Xie, X.; Xu, W.; Liu, X. *Acc. Chem. Res.* **2012**, *45*, 1511−1520.
(11) Castano, A. P.; Mroz, P.; Hamblin, M. R. *Nat. Rev.* **2006**, *6*, 535−545.
(12) Celli, J. P.; Spring, B. Q.; Rizvi, I.; Evans, C. L.; Samkoe, K. S.; Verma, S.; Pogue, B. W.; Hasan, T. *Chem. Rev.* **2010**, *110*, 2795−2838.
(13) Dreaden, E. C.; Mackey, M. A.; Huang, X.; Kang, B.; El-Sayed, M. A. *Chem. Soc. Rev.* **2011**, *40*, 3391−3404.
(14) Hongying, Y.; Fuyuan, W.; Zhiyi, Z. *Dyes Pigments* **1999**, *43*, 109−117.
(15) Coutier, S.; Mitra, S.; Bezdetnaya, L. N.; Parache, R. M.; Georgakoudi, I.; Foster, T. H.; Guillemin, F. *Photochem. Photobiol.* **2001**, *73*, 297−303.
(16) Tromberg, B. J.; Orenstein, A.; Kimel, S.; Barker, S. J.; Hyatt, J.; Nelson, J. S.; Berns, M. W. *Photochem. Photobiol.* **1990**, *52*, 375−385.
(17) Sitnik, T. M.; Hampton, J. A.; Henderson, B. W. *Br. J. Cancer* **1998**, *77*, 1386−1394.
(18) Huang, X.; Jain, P. K.; El-Sayed, I. H.; El-Sayed, M. A. *Photochem. Photobiol.* **2006**, *82*, 412−417.
(19) Takahashi, H.; Niidome, T.; Nariai, A.; Niidome, Y.; Yamada, S. *Nanotechnology* **2006**, *17*, 4431−4435.
(20) Lu, W.; Singh, A. K.; Khan, S. A.; Senapati, D.; Yu, H.; Ray, P. C. *J. Am. Chem. Soc.* **2010**, *132*, 18103−18114.
(21) Beckham, J. T.; Wilmink, G. J.; Opalenik, S. R.; Mackanos, M. A.; Abraham, A. A.; Takahashi, K.; Contag, C. H.; Takahashi, T.; Jansen, E. D. *Lasers Surg. Med.* **2010**, *42*, 912−925.
(22) Wang, J.; Zhu, G.; You, M.; O'Donoghue, M. B.; Shukoor, M. I.; Zhang, K.; Chen, Y.; Zhu, Z.; Song, E.; Huang, C. Z.; Tan, W. *ACS Nano* **2012**, *6*, 5070−5077.
(23) Wang, J.; You, M.; Zhu, G.; Shukoor, M. I.; Li, C.; Chen, Z.; Zhao, Z.; Altman, M. B.; Yuan, Q.; Zhu, Z.; Chen, Y.; Huang, C. Z.; Tan, W. *Small* **2013**, *9*, 3678−3684.
(24) Wang, S.; Huang, P.; Nie, L.; Xing, R.; Liu, D.; Wang, Z.; Lin, J.; Chen, S.; Niu, G.; Lu, G.; Chen, X. *Adv. Mater.* **2013**, *25*, 3055−3061.
(25) Jang, B.; Park, J.-Y.; Tung, C.-H.; Kim, I.-H.; Choi, Y. *ACS Nano* **2011**, *5*, 1086−1094.
(26) Gao, L.; Fei, J.; Zhao, J.; Li, H.; Cui, Y.; Li, J. *ACS Nano* **2012**, *6*, 8030−8040.
(27) Tian, B.; Wang, C.; Zhang, S.; Feng, L.; Liu, Z. *ACS Nano* **2011**, *5*, 7000−7009.
(28) Guo, M.; Mao, H.; Li, Y.; Zhu, A.; He, H.; Yang, H.; Wang, Y.; Tian, X.; Ge, C.; Peng, Q.; Wang, X.; Yang, X.; Chen, X.; Liu, G.; Chen, H. *Biomaterials* **2014**, *35*, 4656−4666.
(29) Topete, A.; Alatorre-Meda, M.; Iglesias, P.; Villar-Alvarez, E. M.; Barbosa, S.; Costoya, J. A.; Taboada, P.; Mosquera, P. *ACS Nano* **2014**, *8*, 2725−2738.
(30) Chena, Q.; Wanga, C.; Chenga, L.; He, W.; Cheng, Z.; Liu, Z. *Biomaterials* **2014**, *35*, 2915−2923.
(31) Kennedy, L. C.; Bickford, L. R.; Lewinski, N. A.; Coughlin, A. J.; Hu, Y.; Day, E. S.; West, J. L.; Drezek, R. A. *Small* **2011**, *7*, 169−183.
(32) Ye, E.; Win, K. Y.; Tan, H. R.; Lin, M.; Teng, C. P.; Mlayah, Z.; Han, M.-Y. *J. Am. Chem. Soc.* **2011**, *133*, 8506−8509.
(33) Wang, Y.; Black, K. C. L.; Luehmann, H.; Li, W.; Zhang, Y.; Cai, X.; Wan, D.; Liu, S.-Y.; Li, M.; Kim, P.; Li, Z.-Y.; Wang, L. V.; Liu, Y.; Xia, Y. *ACS Nano* **2013**, *7*, 2068−2077.
(34) Hasan, W.; Stender, C. L.; Lee, M. H.; Nehl, C. L.; Lee, J.; Odom, T. W. *Nano Lett.* **2009**, *9*, 1555−1558.
(35) Krpetic, Z.; Nativo, P.; Sée, V.; Prior, I. A.; Brust, M.; Volk, M. *Nano Lett.* **2010**, *10*, 4549−4554.
(36) Pasparakis, G. *Small* **2013**, *9*, 4130−4134.
(37) Minai, L.; Yeheskely-Hayon, D.; Yelin, D. *Sci. Rep.* **2013**, *3*, 2146.
(38) Zhao, T.; Shen, X.; Li, L.; Guan, Z.; Gao, N.; Yuan, P.; Yao, S. Q.; Xu, Q.-H.; Xu, G. Q. *Nanoscale* **2012**, *4*, 7712−7719.
(39) Gao, L.; Liu, R.; Gao, F.; Wang, Y.; Jiang, X.; Gao, X. *ACS Nano* **2014**, *8*, 7260−7271.
(40) Vankayala, R.; Huang, Y.-K.; Kalluru, P.; Chiang, C.-S.; Hwang, K. C. *Small* **2014**, *10*, 1612−1622.
(41) Lim, B.; Xia, Y. *Angew. Chem., Int. Ed.* **2011**, *50*, 76−85.
(42) Tao, A. R.; Habas, S.; Yang, P. *Small* **2008**, *4*, 310−325.
(43) Hao, F.; Nehl, C. L.; Hafner, J. H.; Nordlander, P. *Nano Lett.* **2007**, *7*, 729−732.
(44) Fang, J.; Du, S.; Lebedkin, S.; Li, Z.; Kruk, R.; Kappes, M.; Hahn, H. *Nano Lett.* **2010**, *10*, 5006−5013.
(45) Pradhan, M.; Chowdhury, J.; Sarkar, S.; Sinha, A. K.; Pal, T. *J. Phys. Chem. C* **2012**, *116*, 24301−24313.
(46) Li, Q.; Jiang, Y.; Han, R.; Zhong, X.; Liu, S.; Li, Z.-Y.; Sha, Y.; Xu, D. *Small* **2013**, *9*, 927−932.
(47) Yin, Y.; Alivisatos, P. A. *Nature* **2005**, *437*, 664−670.

(48) Erlebacher, J.; Aziz, M. J.; Karma, A.; Dimitrov, N.; Sieradzki, K. *Nature* **2001**, *410*, 450−453.
(49) Chen, S.; Wang, Z. L.; Ballato, J.; Foulger, S. H.; Carro, D. L. *J. Am. Chem. Soc.* **2003**, *125*, 16186−16187.
(50) Yamamoto, M.; Kashiwagi, Y.; Sakata, T.; Mori, H.; Nakamoto, M. *Chem. Mater.* **2005**, *17*, 5391−5393.
(51) Wang, Z.; Zhang, J.; Ekman, J. M.; Kenis, P. J. A.; Lu, Y. *Nano Lett.* **2010**, *10*, 1886−1891.
(52) Barbosa, S.; Agrawal, A.; Rodríguez-Lorenzo, L.; Pastoriza-Santos, I.; Alvarez-Puebla, R. A.; Kornowski, A.; Weller, H.; Liz-Marzan, L. M. *Langmuir* **2010**, *26*, 14943−14950.
(53) Lee, H.; Dellatore, S. M.; Miller, W. M.; Messersmith, P. B. *Science* **2007**, *318*, 426−430.
(54) Lynge, M. E.; van der Westen, R.; Postmab, A.; Städler, B. *Nanoscale* **2011**, *3*, 4916−4928.
(55) Lee, B. P.; Messersmith, P. B.; Israelachvili, J. N.; Waite, J. H. *Annu. Rev. Mater. Res.* **2011**, *41*, 99−132.
(56) Weinhold, M.; Soubatch, S.; Temirov, R.; Rohlfing, M.; Jastorff, B.; Tautz, F. S.; Doose, C. *J. Phys. Chem. B* **2006**, *110*, 23756−23769.
(57) Ryu, J.; Ku, S. H.; Lee, H.; Park, C. B. *Adv. Funct. Mater.* **2010**, *20*, 2132−2139.
(58) Fei, B.; Qian, B.; Yang, Z.; Wang, R.; Liu, W. C.; Mak, W. C.; Xin, J. H. *Carbon* **2008**, *46*, 1795−1797.
(59) Ooka, A. A.; Garrell, R. L. *Biopolymers* **2000**, *57*, 92−102.
(60) Dreyer, D. R.; Miller, D. J.; Freeman, B. D.; Paul, D. R.; Bielawski, C. *Langmuir* **2012**, *28*, 6428−6435.
(61) Chen, C.-T.; Ball, V.; de Almeida Gracio, J. J.; Singh, M. K.; Toniazzo, V.; Ruch, D.; Buehler, M. J. *ACS Nano* **2013**, *7*, 1524−1532.
(62) Hong, S.; Na, Y. S.; Choi, S.; Song, I. T.; Kim, W. Y.; Lee, H. *Adv. Funct. Mater.* **2012**, *22*, 4711−4717.
(63) Liu, Y.; Ai, K.; Lu, L. *Chem. Rev.* **2014**, *114*, 5057−5115.
(64) Huang, Y.-F.; Zhang, M.; Zhao, L.-B.; Feng, J.-M.; Wu, D.-Y.; Ren, B.; Tian, Z.-Q. *Angew. Chem., Int. Ed.* **2014**, *53*, 2353−2357.
(65) Vankayala, R.; Sagadevan, A.; Vijayaraghavan, P.; Kuo, C.-L.; Hwang, K. C. *Angew. Chem., Int. Ed.* **2011**, *50*, 10640−10644.
(66) Kawasaki, H.; Kumar, S.; Li, G.; Zeng, C.; Kauffman, D. R.; Yoshimoto, J.; Iwasaki, Y.; Jin, R. *Chem. Mater.* **2014**, *26*, 2777−2788.
(67) Zhao, T.; Shen, X.; Li, L.; Guan, Z.; Gao, N.; Yuan, P.; Yao, S. Q.; Xu, Q.-H.; Xu, G. Q. *Nanoscale* **2012**, *4*, 7712−7719.
(68) Kraljic, I.; Mohsni, S. E. *Photochem. Photobiol.* **1978**, *28*, 577−581.
(69) Huang, X.; Neretina, S.; El-Sayed, M. A. *Adv. Mater.* **2009**, *21*, 4880−4910.
(70) Hessel, C. M.; Pattani, V. P.; Rasch, M.; Panthani, M. G.; Koo, B.; Tunnell, J. W.; Korgel, B. A. *Nano Lett.* **2011**, *11*, 2560−2566.
(71) Cedervall, T.; Lynch, I.; Foy, M.; Berggrd, T.; Donnelly, S. C.; Cagney, G.; Linse, S.; Dawson, K. A. *Angew. Chem., Int. Ed.* **2007**, *46*, 5754−5756.
(72) Alkilany, A. M.; Murphy, C. J. *J. Nanopart. Res.* **2010**, *12*, 2313−2333.
(73) Rosi, N. L.; Giljohann, D. A.; Thaxton, C. S.; Lytton-Jean, A. K. R.; Han, M. S.; Mirkin, C. A. *Science* **2006**, *19*, 1027−1030.
(74) De Paoli Lacerda, S. H.; Park, J. J.; Meuse, C.; Pristinski, D.; Becker, M. L.; Karim, A.; Douglas, J. F. *ACS Nano* **2010**, *4*, 365−379.
(75) Mahmoudi, M.; Lohse, S. E.; Murphy, C. J.; Fathizadeh, A.; Montazeri, A.; Suslick, K. S. *Nano Lett.* **2014**, *14*, 6−12.
(76) O'Neill, K. L.; Fairbairn, D. W.; Smith, M. J.; Poe, B. S. *Apoptosis* **1998**, *3*, 369−375.
(77) van der Zee, J. *Ann. Oncol.* **2002**, *13*, 1173−1184.
(78) Semighini, C. P.; Harris, S. D. *Methods Mol. Biol.* **2010**, *638*, 269−279.
(79) Darland-Ransom, M.; Wang, X.; Sun, C.-L.; Mapes, J.; Gengyo-Ando, K.; Mitani, S.; Xue, D. *Science* **2008**, *320*, 528−531.
(80) Fairn, G. D.; Grinstein, S. A. *Science* **2008**, *320*, 458−460.
(81) Panikkanvalappil, S. R.; Mackey, M. A.; El-Sayed, M. A. *J. Am. Chem. Soc.* **2013**, *135*, 4815−4821.
(82) Panikkanvalappil, S. R.; Mahmoud, M. A.; Mackey, M. A.; El-Sayed, M. A. *ACS Nano* **2013**, *7*, 7524−7533.
(83) Balasubramanian, B.; Pogozelski, W. K.; Tullius, T. D. *Proc. Natl. Acad. Sci. U. S. A.* **1998**, *95*, 9738−9743.
(84) Steenken, S.; Jovanovic, S. V. *J. Am. Chem. Soc.* **1997**, *119*, 617−618.
(85) Cadet, J.; Delatour, T.; Douki, T.; Gasparutto, D.; Pouget, J.-P.; Ravanat, J.-L.; Sauvaigo, S. *Mutat. Res., Fundam. Mol. Mech. Mutagen.* **1999**, *424*, 9−21.